Article

Liquid-like spin dynamics in a hybrid Heisenberg-Ising antiferromagnet

Jin-Kwang Kim[1,2,6], Hoon Kim[1,2,6], Junyoung Kwon[1,2,6], Hyun-Woo J. Kim[1,2], Kwangrae Kim [1,2], Seung-Hyeok Ha[1,2], Jaehwon Kim[1,2], Hyun-Sung Kim[1,2], Jimin Kim [2], Gahee Noh [3], Gi-Yeop Kim [3], Si-Young Choi [3], Jaeku Park [4], Intae Eom [4], Dogeun Jang [4], Sae Hwan Chun [4], Ayman Said[5], XianRong Huang[5], Jungho Kim[5] & B. J. Kim [1,2] ✉

Two-dimensional (2D) materials and their heterostructures enable unconventional electronic properties and functionalities not accessible in their bulk counterparts. This approach is now being extended to magnetic materials to engineer their spin structures and magnetic fields produced by them. However, spin dynamics of 2D magnetic heterostructures remain largely unexplored. Here, we demonstrate that heterointerfacing Heisenberg square-lattice antiferromagnet (AF) Sr_2IrO_4 with its bilayer variant Ising AF $Sr_3Ir_2O_7$ in a superlattice leads to liquid-like spin dynamics in the former, characterized by slow recovery of the AF order after its transient suppression by an optical pump, and complete absence of spin waves except in an immediate vicinity of the ordering wavevector. Instead, the spin excitation spectra are dominated by isotropic continua, which in previous works have been interpreted as fractional spin excitations, or spinons, that extends to unprecedentedly low energies. Thus, our results provide a pathway to frustrated magnetism in square lattices by heterointerfacing two distinct types of AFs.

Spinons are well-established quasiparticles in one-dimensional (1D) systems[1,2], but their presence in dimensions higher than one remains a contentious topic[3,4]. In particular, spin-1/2 Heisenberg AFs on quasi-2D square lattices have been the subject of tremendous research effort in connection with high-temperature superconductivity (HTSC) in cuprates[5]. Despite the presence of Néel AF orders and the absence of apparent frustrations in these systems, earlier theoretical and experimental works have indicated that they can accommodate gapped spinon modes[6-8]. Indeed, the broad continua observed across many copper-based square-lattice AFs[7,9,10], known as the '(π, 0) anomaly', have been attributed to spinon excitations. Theoretically, their weights should increase in systems with enhanced long-range, multi-spin interactions competing with nearest-neighbor (NN) Heisenberg exchange (J)[11,12], such as four-spin exchanges (Q)[8,13,14], which can

destabilize the Néel AF order in favor of more exotic phases. However, these parameters are difficult to control experimentally and the existence of spinons in square lattices remains unsettled.

The realization of spin-orbit-entangled pseudospin-1/2 square-lattice AFs in iridates offers novel material platforms for exploring the problem in an uncharted parameter regime. The strong spin-orbit coupling in iridates imparts unique properties to their exchange interactions, ranging from a nearly isotropic Heisenberg to a bond-directional Ising-like exchange interaction[15]. This leads to a variety of theoretical predictions for novel quantum magnets, including Kitaev spin liquid in honeycomb compounds[15-19], $U(1)$ or Z_2 quantum spin liquid in hyperkagome compounds[20,21]. Similarly, in square-lattice iridates, enhanced higher-order spin interactions from spatially extended 5d orbitals and increased virtual charge fluctuations due to a small

[1]Department of Physics, Pohang University of Science and Technology, Pohang, South Korea. [2]Center for Artificial Low Dimensional Electronic Systems, Institute for Basic Science (IBS), 77 Cheongam-Ro, Pohang, South Korea. [3]Department of Materials Science and Engineering, Pohang University of Science and Technology, Pohang, South Korea. [4]Pohang Accelerator Laboratory, POSTECH, PohangGyeongbukSouth Korea. [5]Advanced Photon Source, Argonne National Laboratory, Argonne, IL, USA. [6]These authors contributed equally: Jin-Kwang Kim, Hoon Kim, Junyoung Kwon. ✉e-mail: bjkim6@postech.ac.kr

charge gap[22] underlie the strong deviation of the single-layer (SL) Sr_2IrO_4 from the NN Heisenberg model[23] and the exceptionally large spin gap in the double-layer (DL) $Sr_3Ir_2O_7$[24,25].

Thus, the nature of exchange interactions in iridates varies widely even within the Ruddlesden-Popper (R-P) series $Sr_{n+1}Ir_nO_{3n+1}$. This allows for the possibility of heterointerfacing different types of magnetism in a superlattice, which may induce magnetic frustration through proximity coupling of symmetry-distinct orders[26]. In this article, we demonstrate a heterostructure-based strategy to frustrate the Néel AF order in square-lattice iridates. We use time-resolved resonant x-ray diffraction (RXD) to measure the degree of quantum fluctuations through the recovery dynamics of the AF order after its transient suppression by an optical pump, which significantly slows down with enhanced frustration. We use polarization-resolved resonant inelastic x-ray scattering (RIXS) and high-energy-resolution RIXS to reveal the absence of single magnons in most part of the Brillouin zone away from the immediate vicinity of the ordering wavevector. Instead, the spectra are dominated by isotropic continua, which

provide compelling evidence for spinons in a square-lattice Heisenberg AF.

Results

Scanning transmission electron micrososcpy

The recently discovered $n = 1.5$ member of the R-P series[27] is a "natural" superlattice, which can be grown in a single-crystalline form using the flux method. Figure 1a displays the crystal and magnetic structures of Sr_2IrO_4, $Sr_3Ir_2O_7$, and $Sr_5Ir_3O_{11}$, corresponding to $n = 1$, 2 and 1.5 in the R-P series, respectively. Sr_2IrO_4 exhibits an in-plane canted AF order in the SL square lattice[28], whereas the DL square lattice $Sr_3Ir_2O_7$ is characterized by a c-axis collinear AF order[29]. $Sr_5Ir_3O_{11}$ features an alternating stacking of SL and DL, preserving the magnetic structures as well as the gross features in the excitation spectra of the parent compounds[27]. The lattice structures of these three compounds are investigated by scanning transmission electron microscopy (STEM), as shown in Fig. 1b. The images taken along the [100] direction clearly reveal the alternating pattern of SL and DL stackings in $Sr_5Ir_3O_{11}$ as well
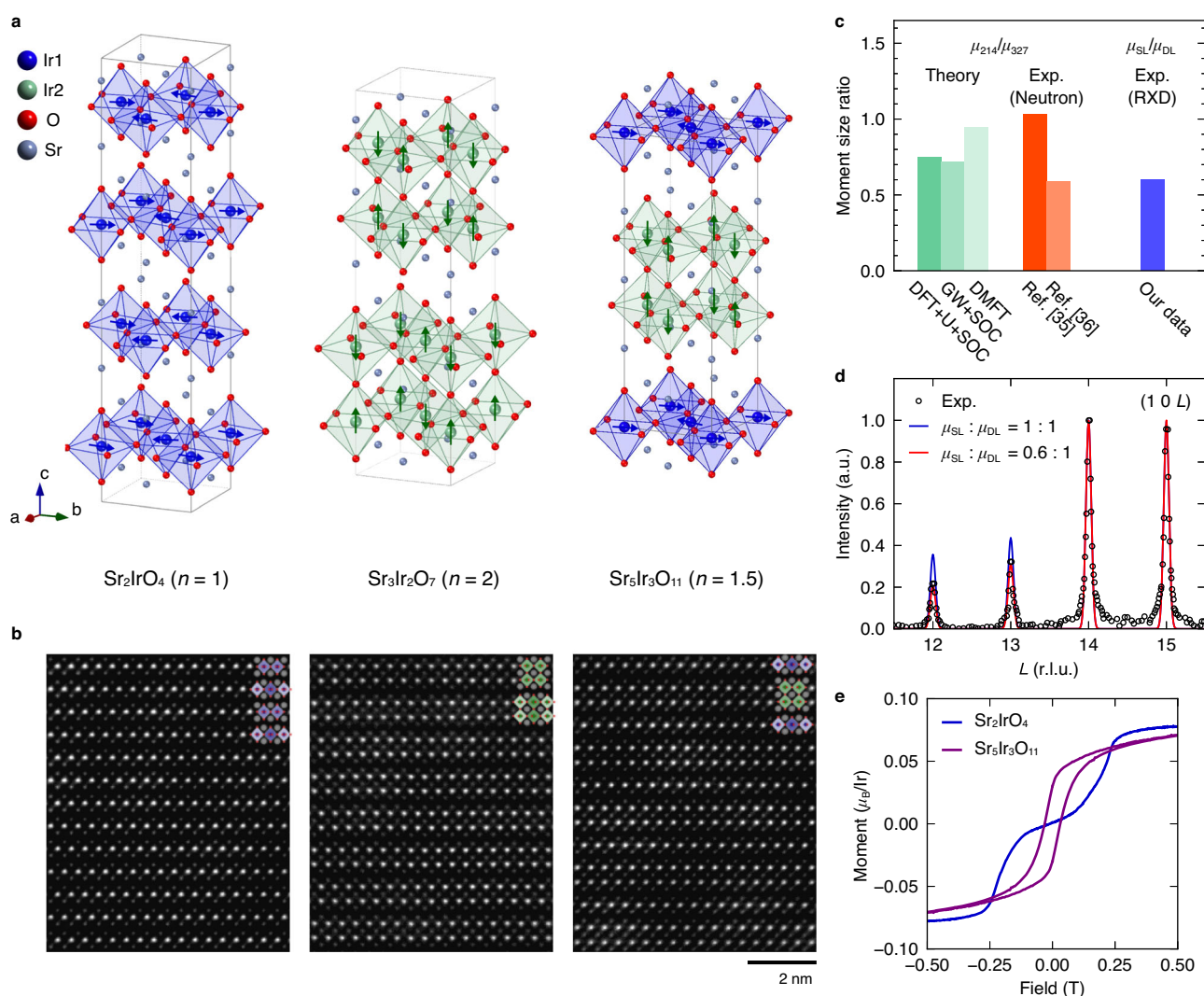

Fig. 1 | Crystal and magnetic structures of square-lattice iridates. a Crystal and magnetic structures of R-P series iridates. Unit cells are indicated by gray lines. Iridium ions and IrO_6 octahedra in SL (DL) are colored blue (green). **b** Stacking patterns of R-P series iridates revealed in STEM images taken along the [100] projection, with corresponding structural models superimposed in the upper right corner of each panel. **c** The ratio of the ordered moment size of Sr_2IrO_4 to that of $Sr_3Ir_2O_7$ (μ_{214}/μ_{327}), based on estimations from theoretical[30–34] and experimental[35–37] studies. This is compared to the ratio of the ordered moment size of SL to that of DL in $Sr_5Ir_3O_{11}$ (μ_{SL}/μ_{DL}), which is measured directly in our RXD experiment shown in (**d**). **d** (1 0 L) scan of magnetic Bragg reflections of $Sr_5Ir_3O_{11}$. The simulation for $\mu_{SL}/\mu_{DL} = 0.6$ (red line) is in good agreement with the experimental data (black circles). Numerical simulations are convoluted with a Gaussian function to account for the experimental momentum resolution and the finite correlation length of the AF order along the L direction. **e** Magnetization measurements of Sr_2IrO_4 and $Sr_5Ir_3O_{11}$ adapted from Ref. 27. The induced moment size of $Sr_5Ir_3O_{11}$ at 0.5 T is smaller than that of Sr_2IrO_4 by a factor of ≈ 0.9.
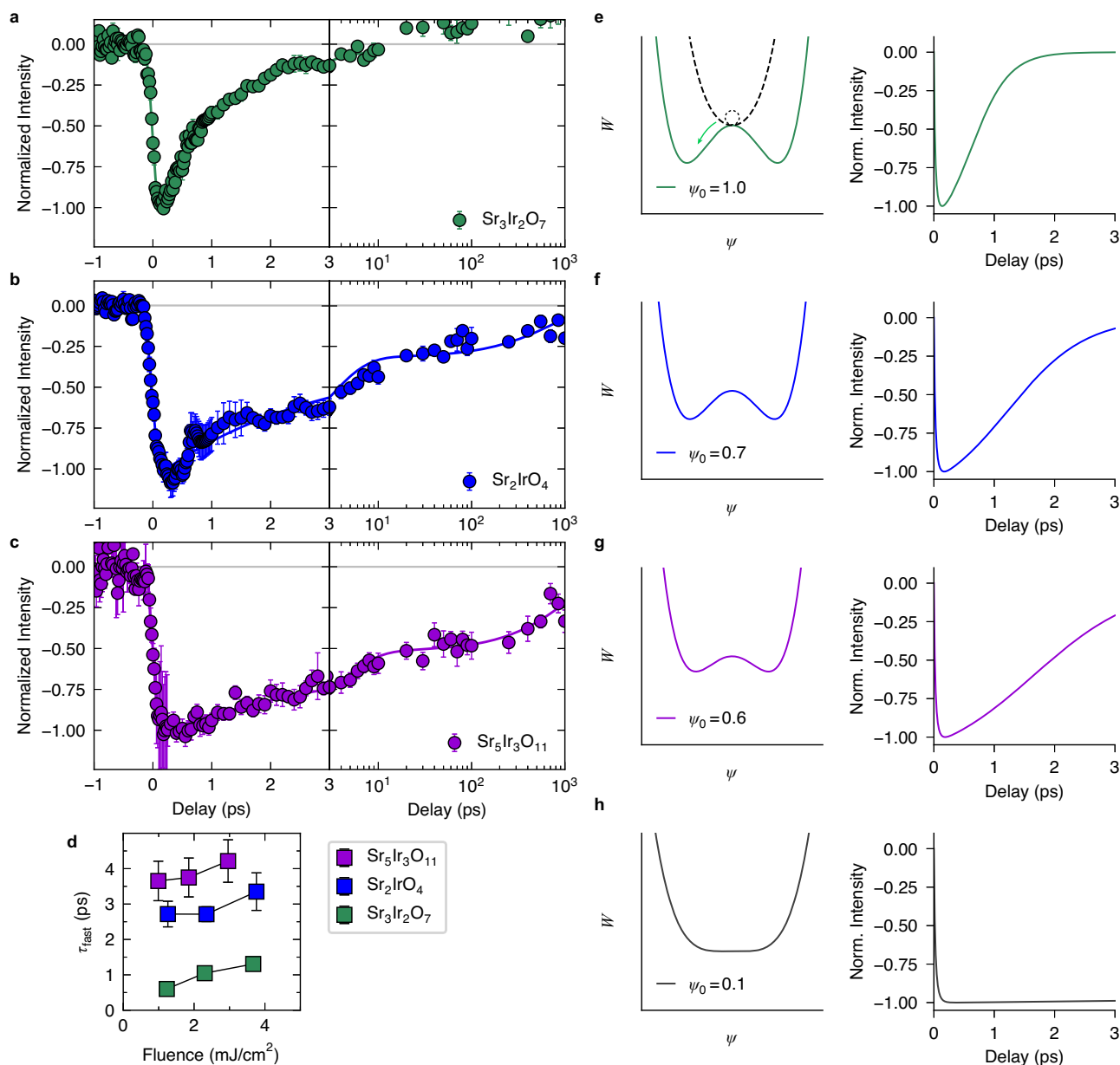
Fig. 2 | Recovery dynamics of AF orders after optical stimulation. Delay curves (circles) for $Sr_3Ir_2O_7$ (**a**), Sr_2IrO_4 (**b**), and $Sr_5Ir_3O_{11}$ (**c**), with corresponding fitted curves (solid lines) spanning from −1 to 1000 ps, separated into fast (-1 to 3 ps) and slow (3 to 1000 ps) timescales. The latter is plotted on a logarithmic scale. The data for pump fluence of 2.30, 2.35 and 1.85 mJ/cm² are shown for $Sr_3Ir_2O_7$, Sr_2IrO_4 and $Sr_5Ir_3O_{11}$, respectively. Error bars indicate the standard deviations from multiple measurements. The magnetic reflection of $Sr_5Ir_3O_{11}$ is measured at (−1 0 8) to minimize the DL contribution[27]. The intensities of delay curves are normalized to −1 at their minima. **d** Pump fluence dependence of the fast recovery time constants. Error bars are the standard errors of the estimated parameters obtained from the fitting. **e**–**h** Transient equilibrium Landau free energies (solid curves) after an optical pump pulse at $t = 0$ (left panel) and time profiles simulated for order parameters for $\psi_0 = 1.0$ (**e**), 0.7 (**f**), 0.6 (**g**), and 0.1 (**h**). The schematic in **e** visualizes the recovery process. The potential well shown by the dashed line represents the Landau free energy immediately after the arrival of an optical pump pulse, leading to the decay of the order parameter. Over several picoseconds, the Landau free energy evolves to a transient equilibrium state (solid curves) with partial recovery of the AF order (solid green arrow).

as the stacking patterns of SL and DL in Sr_2IrO_4 and $Sr_3Ir_2O_7$, respectively.

Resonant x-ray diffraction

For these three compounds, Fig. 1c–e compare the sizes of the ordered magnetic moments, which depend on many factors such as Ir $5d$–O $2p$ hybridization, IrO_6 octahedra distortions, thermal and quantum fluctuations. Although the estimated values from both theory[30,31,31–34] and experiment[35–37] are widely scattered, an overall trend is that the moment size is smaller in Sr_2IrO_4 as compared to $Sr_3Ir_2O_7$ (Fig. 1c).

While this is expected because of stronger quantum fluctuations in the Heisenberg Sr_2IrO_4, we note that this effect is not captured in density functional theory based calculations. Our RXD result on $Sr_5Ir_3O_{11}$ allows for a direct comparison of the moment sizes in SL and DL in $Sr_5Ir_3O_{11}$. Figure 1d shows the intensity measured along (1 0 L) at the base temperature of 10 K. Both SL and DL contribute to magnetic Bragg reflections at every integer L, but their contributions can be separated by exploiting the fact that the DL contribution to the intensity oscillates due to its structure factor as $\cos^2(2\pi d/c)$[27,29], where d is the distance between the two layers comprising DL and c is

the c-axis lattice parameter, whereas SL contributes a nearly constant intensity. The L dependence of the intensity can be reproduced by a simple model (see Supplementary Note 1), from which we estimate the SL moment size to be $\approx 60\%$ of that of DL. Thus, our data reveal much stronger quantum fluctuations in SL relative to DL, assuming that other aforementioned factors do not differ significantly between SL and DL. Next, we compare the ordered moment size of SL in $Sr_5Ir_3O_{11}$ to that in Sr_2IrO_4 (Fig. 1e). Because DL does not contribute to the net magnetization and the octahedra rotation angles are almost the same for the two compounds (see Supplementary Note 2), the moment sizes can be estimated through the net magnetization from the canting of the moments. We estimate the SL moment size in $Sr_5Ir_3O_{11}$ to be around 90% of that in Sr_2IrO_4, indicating further reduction of the ordered moment by heterointerfacing. Although this may appear to be a small effect, we shall see below that it has a dramatic effect in the spin dynamics.

Time-resolved resonant x-ray diffraction

To provide further evidence for the magnetic frustration, we employ time-resolved RXD to follow the recovery of the AF order after its transient suppression induced by an optical pump pulse. Figure 2a–c compare the decay and recovery dynamics of $Sr_3Ir_2O_7$, Sr_2IrO_4 and $Sr_5Ir_3O_{11}$, respectively. $Sr_5Ir_3O_{11}$ is measured at $\mathbf{q} = (-1\,0\,8)$ to minimize the contribution of DL[27]. For a quantitative analysis, the delay curves are fitted by a double exponential relaxation function $f(t)$ expressed as[38]

$$
f(t) = -\left[\frac{1}{2}\left(1 + \mathrm{Erf}\left(\frac{2\sqrt{2}(t - t_0)}{\tau_{\mathrm{decay}}}\right)\right) \\ \times \left(Ae^{-(t - t_0)/\tau_{\mathrm{fast}}} + Be^{-(t - t_0)/\tau_{\mathrm{slow}}}\right)\right],
$$

(1)

where t_0 denotes the arrival time of an optical pump pulse and τ_{decay} refers to the decay time of magnetic Bragg reflections. A and B represent the intensities recovered on two different timescales: τ_{fast}, representing the build-up of 2D correlations in a few ps, and τ_{slow}, representing a slower recovery of 10-100 ps timescale associated with restoration of three-dimensional (3D) correlations[38]. The decay process is fitted by the error(Erf) function. We fit the delay curves of $Sr_3Ir_2O_7$ only below 5 ps with a single exponential relaxation function (Fig. 2a) as in the previous work[39], which corresponds to $B = 0$ in Eq. (1), because extrinsic effects such as strain waves come into play beyond 10 ps, leading to an overshoot in the intensity of the $Sr_3Ir_2O_7$ curve[39]. The extracted time constants for Sr_2IrO_4 and $Sr_3Ir_2O_7$ align with those from previous studies[38,39] (see Supplementary Note 3). We shall concern ourselves with τ_{fast} only as it is relevant to intraplane processes, and its fitted values are shown in Fig. 2d for various fluences from 1 to 4 mJ/cm².

$Sr_3Ir_2O_7$ exhibits a significantly faster 2D recovery (τ_{fast}) compared to Sr_2IrO_4 and $Sr_5Ir_3O_{11}$, with $Sr_5Ir_3O_{11}$ showing a slightly but clearly slower recovery than Sr_2IrO_4 for all fluences measured. The rapid 2D recovery observed in $Sr_3Ir_2O_7$ is attributed to its Ising-type order, which has negligible quantum fluctuations. On the other hand, the longer τ_{fast} signifies an enhanced frustration in the SL of $Sr_5Ir_3O_{11}$. We demonstrate this in Figs. 2e–h, using a phenomenological time-dependent Ginzburg-Landau theory (see Supplementary Note 4). In our simulation, the order parameter ψ_0 are chosen to approximately match the relative moment sizes estimated in Fig. 1c–e: $\psi_0 = 1.0$ for $Sr_3Ir_2O_7$ (Fig. 2e), 0.7 for Sr_2IrO_4 (Fig. 2f), and 0.6 for $Sr_5Ir_3O_{11}$ (Fig. 2g). ψ_0 becomes zero as the electron temperature is instantaneously raised by the optical pump pulse, and subsequently recovers transient equilibrium value as heat is transferred to the lattice over a few ps timescale. The recovery process slows down when ψ_0 is reduced and the potential well becomes shallow, semiquantitatively reproducing the experimental results in Fig. 2a–c. These results imply that enhanced

magnetic frustration can manifest as slower recovery dynamics of magnetic Bragg reflections. In an extreme case where ψ_0 approaches zero near the critical point, the recovery time diverges (Fig. 2h).

Resonant inelastic x-ray scattering

Armed with this information, we now address the long-standing issue of the origin of $(\pi, 0)$ anomaly in square-lattice AFs. Figure 3 shows polarization-resolved RIXS measurements on Sr_2IrO_4 and $Sr_5Ir_3O_{11}$. Although resolving the polarization of scattered x-ray is not currently feasible for hard x-ray RIXS, the polarizations of spin waves can be resolved by measuring the same $\mathbf{q}$ points in several different geometries (Ref. 40 and Supplementary Note 5). For Sr_2IrO_4 (Fig. 3a), the $(\pi, 0)$ spectrum exhibits identical transverse (T) and longitudinal (L) responses, as revealed in our previous study[40]; i.e. the spectra are isotropic with no visible trace of single magnons, which should appear exclusively in the T channel. In contrast, the T spectrum at $(\pi/2, \pi/2)$ displays a well-defined single magnon, superimposed on a broad feature that appears in both channels. In between these two points, polarization analyses show a gradual decay of single magnon into isotropic continua.

More striking are the spectra of $Sr_5Ir_3O_{11}$ (Fig. 3b), in which the anomaly is not limited to $(\pi, 0)$ but spans the entire zone boundary. Although it is difficult to isolate the spin components of SL at the zone boundary, where the energies of the SL and DL magnons are close to each other[27], there is no ambiguity in resolving the T and L components of SL, because DL contributes a common background for both channels (See Supplementary Note 5). The sharp peak observed at $(\pi/2, \pi/2)$ is identified as the DL magnon mode by comparison with the spectra of $Sr_3Ir_2O_7$ (Supplementary Fig. 6). Within our error bars, we observe no hint of single magnons from SL; the spectra are isotropic along the entire zone boundary. These isotropic continua carry significant spectral weight even very close to the zone center (Fig. 3d), where SL and DL modes are clearly separated in energy. This is in stark contrast with the (π, π) spectrum of Sr_2IrO_4, which is dominated by T single magnons (Fig. 3c).

As the SL mode in $Sr_5Ir_3O_{11}$ is well separated from the DL mode in energy near the zone center (π, π), we use a high-energy-resolution setup ($\Delta E \approx 10$ meV) to measure RIXS spectra near (π, π). Figure 4a compares the low-energy excitations of Sr_2IrO_4 and $Sr_5Ir_3O_{11}$ near the zone center at $(x\pi, x\pi)$ ($x = 0.99$ to 0.92), where both samples are measured under the same experimental conditions. At $x = 0.99$, the peak in $Sr_5Ir_3O_{11}$ is already not quite resolution-limited, whereas Sr_2IrO_4 exhibits a resolution limited single peak. At momenta further away from (π, π), the spectra of $Sr_5Ir_3O_{11}$ exhibit a two-peak-like structure, which is clearly resolved at $x = 0.94$ and 0.92. Because we are not able to perform polarization analysis in the high-energy-resolution setup, and for the lack of an accurate theoretical model to fit the spectra, we provide a phenomenological description by fitting the spectra to two pseudo-Voigt functions, labeling them as 'Peak 1' and 'Peak 2'. Figure 4b presents the 2D color plot of the high-energy-resolution RIXS of $Sr_5Ir_3O_{11}$ from Fig. 4a, overlaid with the dispersions extracted from the fittings. The separation of Peaks 1 and 2 increases linearly with the distance from (π, π), representing the expanding energy range over which the spectral intensity is distributed. Clearly, the spectra of $Sr_5Ir_3O_{11}$ has an extra component that cannot be accounted for by a single magnon excitation.

Discussion

Although the broad high-energy continua observed in $S = 1/2$ square-lattice AFs have often been attributed to spinon excitations[7–10], there are other interpretations in terms of multi-magnons[41,42]. Strong magnon-magnon interactions have been shown to give rise to the formation of two-magnon "Higgs resonances" corresponding to a longitudinal magnon with finite lifetime. In addition, vertex corrections of effective observables lead to three-magnon continuum
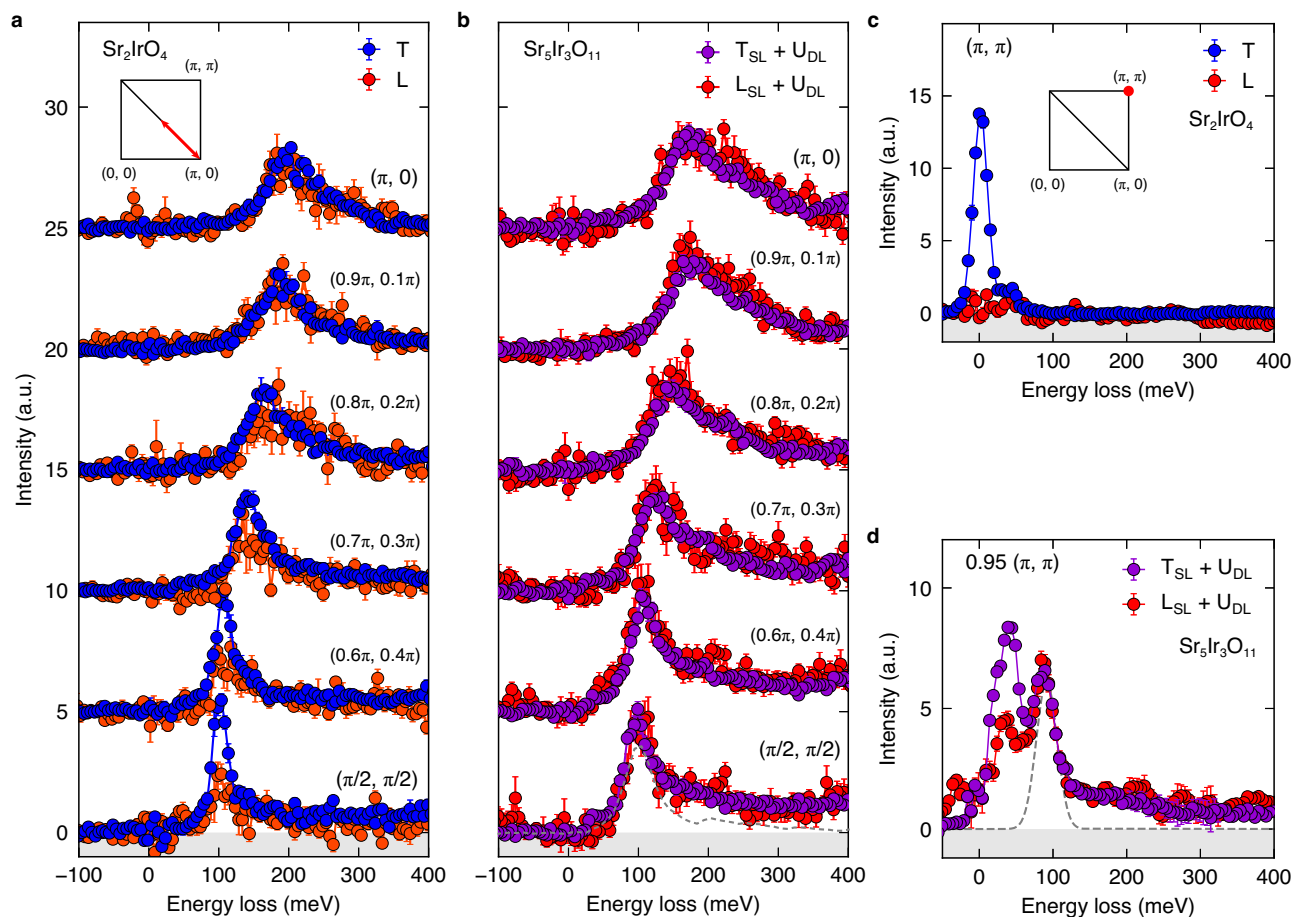
Fig. 3 | Absence of magnons in polarization-resolved RIXS spectra.
a Polarization-resolved spectra of Sr_2IrO_4 along the magnetic zone boundary from $(\pi/2, \pi/2)$ to $(\pi, 0)$, adapted from Ref. 40. Transverse (T) and longitudinal (L) components to the ordered magnetic moments are resolved. The inset shows a quadrant of the Brillouin zone, with the measured wave vectors highlighted by a red line. **b** Polarization-resolved spectra of $Sr_5Ir_3O_{11}$ along the magnetic zone boundary. T_{SL} and L_{SL} denote the transverse and longitudinal components of SL, respectively, while U_{DL} represents the polarization-unresolved background from DL. For the

spectrum at $(\pi/2, \pi/2)$, the contribution from the transverse component of $Sr_3Ir_2O_7$ (Supplementary Fig. 6a) is indicated by a gray dashed line. **c** Polarization-resolved spectra of Sr_2IrO_4 at (π, π). The inset shows a quadrant of the Brillouin zone, with the measured wave vector highlighted by a red dot. **d** Polarization-resolved spectra of $Sr_5Ir_3O_{11}$ at $0.95(\pi, \pi)$. The gray dashed line indicates the single magnon of DL in U_{DL} extracted from fitting. The error bars are calculated through error propagation from the standard deviations of the raw spectra.

excitations in transverse channels[42]. In fact, the spectra of $Sr_3Ir_2O_7$ reveal high-energy features in both transverse and longitudinal channels (Supplementary Fig. 6).

However, the spectra of $Sr_5Ir_3O_{11}$ are inconsistent with the multi-magnon scenario in the following two aspects. First, the continua in transverse and longitudinal channels have different structures in $Sr_3Ir_2O_7$, whereas they are identical in $Sr_5Ir_3O_{11}$. In the multi-magnon scenario, transverse (longitudinal) continuum involves odd(even) number of magnons, and thus their spectra in general have different structures. Second, even after taking into account magnon-magnon interactions and vertex corrections, deviation from the linear spin-wave theory is marginal for low-energy magnons near the zone center, and different theoretical approaches (quantum Monte Carlo[43], series expansion[44], continuous similarity transformation[41,42]) agree with one another, consistent with the result for Sr_2IrO_4 (Fig. 3c).

Therefore, we conclude that the low-energy continua observed in $Sr_5Ir_3O_{11}$ cannot be multi-magnons. Thus, we provide below an interpretation based on the spinon scenario. The 3D plots in Fig. 4c summarize the results of RIXS experiments displayed in Fig. 3. They show the momentum distribution of the coherent single-magnon weights in Sr_2IrO_4 and $Sr_5Ir_3O_{11}$, interpolating the **q**-points between the zone center and boundary. For Sr_2IrO_4, a coherent single magnon completely vanishes only at $(\pi, 0)$, while for $Sr_5Ir_3O_{11}$ it completely breaks

down not only at $(\pi, 0)$ but across the entire zone boundary, with reduced weights even very close to (π, π). We attribute these results to a smaller spinon gap in $Sr_5Ir_3O_{11}$ compared to Sr_2IrO_4, as illustrated in Fig. 4d, induced by increased frustration in SL of $Sr_5Ir_3O_{11}$.

In the *J*-*Q* model with a four-spin exchange *Q*, a spinon branch or a lower edge of the two-spinon continuum has a dispersion given by[8]

$$\omega^s(\mathbf{q}) = \Delta^s + c^s\sqrt{1 - \cos^2 q_x \cos^2 q_y}, \qquad (2)$$

where c^s is the spinon velocity. The dispersion has its energy minimum at $(\pi, 0)$ as shown in Fig. 4d. The spinon gap Δ^s is expected to decrease as *Q*/*J* increases, which corresponds to greater frustration of the AF order[45–47], and ultimately vanishes at a critical value of *Q*/*J*[8]. In $Sr_5Ir_3O_{11}$, interfacial magnetic couplings between AF orders with distinct symmetries in SL and DL (Fig. 1a) possibly enhance the frustration of the AF order in SL (Fig. 1d, e), increasing the effective *Q*/*J* ratio in the 2D spin model. When the spinon continuum falls below the magnon energy with a smaller spinon gap Δ^s, the coherent magnon peak is washed out due to strong magnon-spinon couplings[8]. Therefore, the complete breakdown of the coherent single-magnon peak at $(\pi, 0)$ in Sr_2IrO_4 is due to an overlapping of magnon and spinon branches occurring only at this wave vector, as illustrated in the left panel of Fig. 4d. In contrast, for $Sr_5Ir_3O_{11}$, a small spinon gap Δ_s leads to the breakdown of the

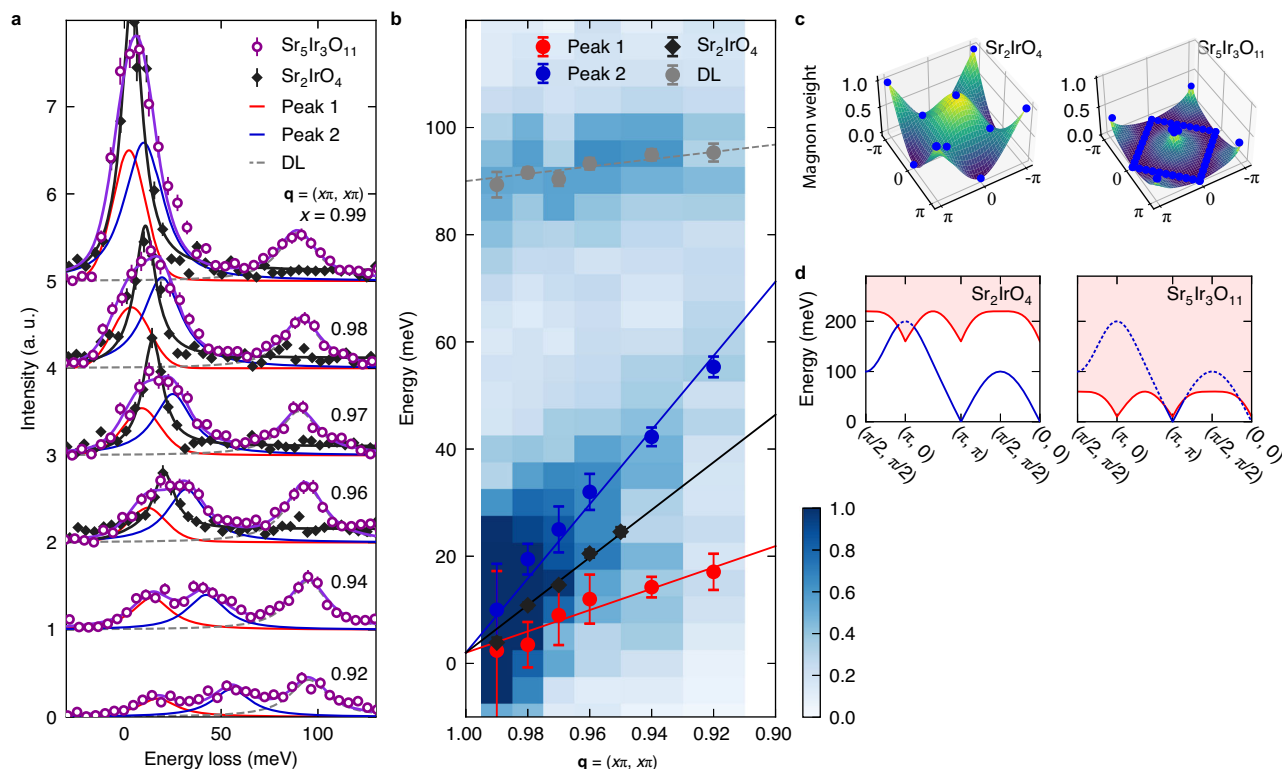**Fig. 4 | Additional mode in high-energy-resolution RIXS spectra. a** Comparison of spectra for $Sr_5Ir_3O_{11}$ and Sr_2IrO_4 near the zone center (π, π). Low energy data for $Sr_5Ir_3O_{11}$ (Sr_2IrO_4) are fitted using two (one) pseudo-Voigt peaks, shown as solid red and blue (black) lines. DL single magnons are fitted by the peaks in gray dashed lines. Error bars denote square roots of the absolute intensities. **b** 2D color plot of the high-energy-resolution RIXS spectra of $Sr_5Ir_3O_{11}$ near the zone center, overlaid with peak positions extracted from the fits in **a**. `Peak 1' (red circles) and `Peak 2' (blue circles) are used to follow the excitations of $Sr_5Ir_3O_{11}$. The single magnon dispersion of Sr_2IrO_4 is marked by black circles. A magnetic mode around 90 meV corresponds to DL single magnon in $Sr_5Ir_3O_{11}$, which mirrors the single magnon mode of $Sr_3Ir_2O_7$[24,27]. Solid lines are linear fits to the peak positions. Error bars

represent the standard error of the estimated parameters obtained from the fitting. **c** Ratio of coherent single-magnons to the total magnetic spectral weight throughout the Brillouin zone for Sr_2IrO_4 (left panel) and $Sr_5Ir_3O_{11}$ (right panel), as estimated from the RIXS measurements in Fig. 3. Data points are marked as blue dots on the surfaces generated by interpolating them. **d** Schematic of magnon dispersion and low energy edge of spinon continua for Sr_2IrO_4 (left panel) and $Sr_5Ir_3O_{11}$ (right panel). Two-spinon continuum is marked by the pink shaded area and the red line represents the lower bound of the continuum, as given by Eq. (2). The blue line represents the single-magnon dispersion extracted by fitting the data shown in Supplementary Fig. 7 using the J-Q model. The dashed part of blue lines indicates the decay of single magnons due to strong magnon-spinon couplings.

coherent single-magnon across the zone boundary, as illustrated in the right panel of Fig. 4d.

Our work demonstrates an effective materials strategy for inducing magnetic frustration in square lattices by exploiting the diverse array of anisotropic interactions displayed by iridates and combining them in one material, providing compelling evidence for unconventional spin excitations in square-lattice AFs. The strong decay of single magnons even at very low energies is unprecedented in earlier works on cuprate square-lattices[7,9,10], where the anomalous continua are confined to high energies. The fully isotropic spectra discovered in square-lattice iridate AFs are thus consistent with quantum-spin-liquid-like spin entanglement in the Néel AF ordered phase[7]. Thus, our findings represent a significant advance toward understanding the quantum spin dynamics in a quasi-2D square-lattice $S = 1/2$ Heisenberg AF. We expect that our work will stimulate further investigations into heterostructure-based approaches to frustrated magnetism in square-lattice iridates using layer-by-layer growth techniques[48–52].

Methods
Sample synthesis
High-quality single crystals of Sr_2IrO_4, $Sr_3Ir_2O_7$, and $Sr_5Ir_3O_{11}$ were grown by the standard flux growth method as described in refs. 27,53 and characterized by Raman spectroscopy and x-ray diffraction.

STEM
STEM measurements were conducted using JEM-ARM200F, JEOL at 200 kV with fifth-order probe-corrector (ASCOR, CEOS GmbH, Germany) at the Materials Imaging & Analysis Center of POSTECH in South Korea. The specimens were prepared by a dual-beam focused ion beam with Ga ion beams of 30 kV (Nanolab G3 CX, FEI) and further milled by Ar ion beams of 100 meV (PIPS II, Gatan) to minimize the surface damage using Precision Ion Polishing System (PIPS II Pro 695, Gatan) at the Materials Imaging & Analysis Center of POSTECH in South Korea.

Time-resolved RXD measurements
Time-resolved RXD was performed at the XSS beamline of the PAL-XFEL with a 60 Hz pulse repetition rate. The incident x-ray beam was tuned to the Ir L_3-edge at 11.215 keV. The time delay curves of Sr_2IrO_4 and $Sr_3Ir_2O_7$ were measured at (-1 0 16) and at (-1 0 13), respectively, in a vertical scattering geometry with grazing incidences. A Jungfrau area detector was used for collecting magnetic Bragg reflection signals. The laser pump pulses of 2.0 μm was injected at an angle of 12° with respect to the x-ray pulses. The x-rays were focused by compound refractive lenses down to 20×20 μm^2 FHWM and the laser spot size was 250 μm FWHM. The temporal resolution of the experiment was measured to be about 300 fs obtained from the delay curve of the (1 1 1) charge-density-wave reflection of a Bi(1 1 1) thin film. All time-resolved RXD

measurements were conducted at $T \approx 100$ K using a cryostream with liquid nitrogen.

Polarization-resolved RIXS

Polarization-resolved RIXS experiments were performed at the 27-ID-B beamline of the Advanced Photon Source. Combining a diamond(1 1 1) high-heat-load monochromator and a two-bounce Si(8 4 4) channel-cut monochromator, the incident x-ray beam was tuned to the Ir L_3-edge (11.215 keV) with the energy bandpass of 14.8 meV. The beam was then focused by a set of Kirkpatrick-Baez mirrors, producing a spot size of 40×10 (H × V) μm^2 FWHM at the sample position. Scattered photons were analyzed by a Si(8 4 4) diced spherical analyzer with a curvature of 2 m radius and with a mask of 2 cm diameter. The total instrumental energy resolution was about 30 meV. A horizontal scattering geometry was used with the incident π-polarization and the outgoing polarization was not resolved. The scattering angle (2θ) was kept around 90° to suppress elastic Thomson scatterings. For Sr_2IrO_4 and $Sr_5Ir_3O_{11}$, an external magnetic field were applied to align the pseudospins along specific directions. More detailed information is provided in Supplementary Note 5.

High-energy-resolution RIXS

High-energy-resolution RIXS were performed at the 27-ID-B beamline of the Advanced Photon Source, employing similar setups as in the polarization-resolving setup, but using different second-monochromator and analyzer. A four-bounce Si (8 4 4) channel-cut monochromator was utilized to narrow the energy bandpass of the incident x-rays to 9 meV. Scattered photons were analyzed by a quartz (3 0 9) diced spherical analyzer with a curvature of 2 m radius and with a mask of 1 cm diameter. This setup achieved an overall energy resolution of 10 meV.

RXD and preliminary RIXS

RXD and preliminary RIXS measurements were performed at the 1C beamline of the Pohang Light Source-II[54]. Using Si (1 1 1) double-crystal monochromator, the incident x-ray beam was tuned to the Ir L_3-edge (11.215 keV) with the energy bandpass about 1 eV. For RIXS experiments, additional two-bounce Si (8 4 4) channel-cut monochromator was installed to reduce the energy bandpass down to 15.8 meV. The beam was then focused by a set of Kirkpatrick-Baez mirrors, yielding a spot size of 25×5 (H × V) μm^2 FWHM at the sample position. In RXD experiments, scattered photons were filtered by a Si (8 4 4) bent analyzer with a curvature of 1 m radius and collected using a DECTRIS EIGER2 2D area x-ray detector to suppress background signals. In RIXS experiments, scattered photons were analyzed by a Si (8 4 4) diced spherical analyzer with a curvature of 1 m radius and collected using a DECTRIS MYTHEN2 1D x-ray detector. The total instrumental energy resolution of preliminary RIXS was about 40 meV.

Data availability

The data supporting the findings are presented in the article and the Supplementary Information. Source data are provided with this paper.

References

1. Tennant, D. A., Cowley, R. A., Nagler, S. E. & Tsvelik, A. M. Measurement of the spin-excitation continuum in one-dimensional $KCuF_3$ using neutron scattering. *Phys. Rev. B* **52**, 13368–13380 (1995).
2. Mourigal, M. et al. Fractional spinon excitations in the quantum Heisenberg antiferromagnetic chain. *Nat. Phys.* **9**, 435–441 (2013).
3. Anderson, P. W. Resonating valence bonds: a new kind of insulator? *Mater. Res. Bull.* **8**, 153–160 (1973).
4. Lee, P. A., Nagaosa, N. & Wen, Xiao-Gang Doping a mott insulator: physics of high-temperature superconductivity. *Rev. Mod. Phys.* **78**, 17–85 (2006).
5. Keimer, B., Kivelson, S. A., Norman, M. R., Uchida, S. & Zaanen, J. From quantum matter to high-temperature superconductivity in copper oxides. *Nature* **518**, 179–186 (2015).
6. Balents, L., Fisher, M.P. A. & Nayak, C. Dual order parameter for the nodal liquid. *Phys. Rev. B* **60**, 1654–1667 (1999).
7. Dalla P, B. et al. Fractional excitations in the square-lattice quantum antiferromagnet. *Nat. Phys.* **11**, 62–68 (2015).
8. Shao, H. et al. Nearly deconfined spinon excitations in the square-lattice Spin-1/2 Heisenberg antiferromagnet. *Phys. Rev. X* **7**, 041072 (2017).
9. Headings, N. S., Hayden, S. M., Coldea, R. & Perring, T. G. Anomalous high-energy spin excitations in the high-T_c superconductor-parent antiferromagnet La_2CuO_4. *Phys. Rev. Lett.* **105**, 247001 (2010).
10. Martinelli, L. et al. Fractional spin excitations in the infinite-layer cuprate $CaCuO_2$. *Phys. Rev. X* **12**, 021041 (2022).
11. Mambrini, M., Läuchli, A., Poilblanc, D. & Mila, F. Plaquette valence-bond crystal in the frustrated heisenberg quantum antiferromagnet on the square lattice. *Phys. Rev. B* **74**, 144422 (2006).
12. Ferrari, F. & Becca, F. Gapless spin liquid and valence-bond solid in the J_1-J_2 Heisenberg model on the square lattice: insights from singlet and triplet excitations. *Phys. Rev. B* **102**, 014417 (2020).
13. Chubukov, A., Gagliano, E. & Balseiro, C. Phase diagram of the frustrated spin-1/2 Heisenberg antiferromagnet with cyclic-exchange interaction. *Phys. Rev. B* **45**, 7889–7898 (1992).
14. Chatterjee, S., Sachdev, S. & Scheurer, M. S. Intertwining topological order and broken symmetry in a theory of fluctuating spin-density waves. *Phys. Rev. Lett.* **119**, 227002 (2017).
15. Jackeli, G. & Khaliullin, G. Mott insulators in the strong spin-orbit coupling limit: from heisenberg to a quantum compass and Kitaev models. *Phys. Rev. Lett.* **102**, 017205 (2009).
16. Chaloupka, J, Jackeli, G. & Khaliullin, G. Kitaev-Heisenberg model on a honeycomb lattice: possible exotic phases in iridium oxides A2IrO3. *Phys. Rev. Lett.* 105, 027204 (2010)..
17. Chun, S.H. et al. Direct evidence for dominant bond-directional interactions in a honeycomb lattice iridate Na_2IrO_3. *Nat. Phys.* **11**, 462–466 (2015).
18. Witczak-Krempa, W., Chen, G., Kim, YongBaek & Balents, L. Correlated quantum phenomena in the strong spin-orbit regime. *Annu. Rev. Condens. Matter Phys.* **5**, 57–82 (2014).
19. Rau, J. G., Lee, E.K.-H. & Kee, H.-Y. Spin-orbit physics giving rise to novel phases in correlated systems: iridates and related materials. *Annu. Rev. Condens. Matter Phys.* **7**, 195–221 (2016).
20. Okamoto, Y., Nohara, M., Aruga-Katori, H. & Takagi, H. Spin-liquid state in the S = 1/2 hyperkagome antiferromagnet $Na_4Ir_3O_8$. *Phys. Rev. Lett.* **99**, 137207 (2007).
21. Takayama, T. et al. Spin-orbit coupling induced semi-metallic state in the 1/3 hole-Doped Hyper-Kagome $Na_3Ir_3O_8$. *Sci. Rep.* **4**, 6818 (2014).
22. Moon, S. J. et al. Dimensionality-controlled insulator-metal transition and correlated metallic state in 5*d* transition metal oxides $Sr_{n+1}Ir_nO_{3n+1}$ (n = 1, 2, and ∞). *Phys. Rev. Lett.* **101**, 226402 (2008).
23. Kim, J. et al. Magnetic excitation spectra of Sr_2IrO_4 probed by resonant inelastic X-ray scattering: establishing links to cuprate superconductors. *Phys. Rev. Lett.* **108**, 177003 (2012).
24. Kim, J. et al. Large spin-wave energy gap in the bilayer iridate $Sr_3Ir_2O_7$: evidence for enhanced dipolar interactions near the mott metal-insulator transition. *Phys. Rev. Lett.* **109**, 157402 (2012).
25. Moretti S, M. et al. Evidence of quantum dimer excitations in $Sr_3Ir_2O_7$. *Phys. Rev. B* **92**, 024405 (2015).

26. Ok, J.M. et al. Frustration-driven C_4 symmetric order in a naturally-heterostructured superconductor Sr_2VO_3FeAs. *Nat. Commun.* **8**, 2167 (2017).

27. Kim, H. et al. $Sr_2IrO_4/Sr_3Ir_2O_7$ superlattice for a model two-dimensional quantum Heisenberg antiferromagnet. *Phys. Rev. Res.* **4**, 013229 (2022).

28. Kim, B. J. et al. Phase-sensitive observation of a spin-orbital mott state in Sr_2IrO_4. *Science* **323**, 1329–1332 (2009).

29. Kim, J. W. et al. Dimensionality driven spin-flop transition in layered iridates. *Phys. Rev. Lett.* **109**, 037204 (2012).

30. Kim, B. J. et al. Novel J_{eff} = 1/2 Mott state induced by relativistic spin-orbit coupling in Sr_2IrO_4. *Phys. Rev. Lett.* **101**, 076402 (2008).

31. Liu, P. et al. Relativistic GW+BSE study of the optical properties of ruddlesden-popper iridates. *Phys. Rev. Mater.* **2**, 075003 (2018).

32. Bhandari, C., Popović, Z. S. & Satpathy, S. Electronic structure and optical properties of Sr_2IrO_4 under epitaxial strain. *N. J. Phys.* **21**, 013036 (2019).

33. Kim, B., Liu, P. & Franchini, C. Magnetic properties of bilayer $Sr_3Ir_2O_7$: role of epitaxial strain and oxygen vacancies. *Phys. Rev. B* **95**, 024406 (2017).

34. Zhang, H., Haule, K. & Vanderbilt, D. Effective J = 1/2 insulating state in Ruddlesden-Popper iridates: An LDA+DMFT Study. *Phys. Rev. Lett.* **111**, 246402 (2013).

35. Dhital, C. et al. Neutron scattering study of correlated phase behavior in Sr_2IrO_4. *Phys. Rev. B* **87**, 144405 (2013).

36. Ye, F. et al. Magnetic and crystal structures of Sr_2IrO_4: a neutron diffraction study. *Phys. Rev. B* **87**, 140406 (2013).

37. Hogan, T. et al. Structural investigation of the bilayer iridate $Sr_3Ir_2O_7$. *Phys. Rev. B* **93**, 134110 (2016).

38. Dean, M. P. M. et al. Ultrafast energy- and momentum-resolved dynamics of magnetic correlations in the Photo-Doped Mott Insulator Sr_2IrO_4. *Nat. Mater.* **15**, 601–605 (2016).

39. Mazzone, D. G. et al. Laser-induced transient magnons in $Sr_3Ir_2O_7$ throughout the brillouin zone. *Proc. Natl Acad. Sci.* **118**, e2103696118 (2021).

40. Kim, H. et al. Quantum spin nematic phase in a square-lattice iridate. *Nature* **625**, 264–269 (2024).

41. Powalski, M., Uhrig, G. S. & Schmidt, K. P. Roton minimum as a fingerprint of Magnon-Higgs scattering in ordered quantum antiferromagnets. *Phys. Rev. Lett.* **115**, 207202 (2015).

42. Powalski, M., Schmidt, K. P. & Uhrig, G. S. Mutually attracting spin waves in the square-lattice quantum antiferromagnet. *SciPost Phys.* **4**, 001 (2018).

43. Sandvik, A. W. Continuous quantum phase transition between an antiferromagnet and a valence-bond solid in two dimensions: evidence for logarithmic corrections to scaling. *Phys. Rev. Lett.* **104**, 177201 (2010).

44. Igarashi, J. & Nagao, T. Magnetic Excitations in L-edge Resonant Inelastic X-ray Scattering from Cuprate Compounds. *Phys. Rev. B* **85**, 064421 (2012).

45. Majumdar, K., Furton, D. & Uhrig, G. ötzS. Effects of ring exchange interaction on the néel phase of two-dimensional, spatially anisotropic, frustrated heisenberg quantum antiferromagnet. *Phys. Rev. B* **85**, 144420 (2012).

46. Zhou, Z., Wu, C. & Wang, Y. Mott Transition in the π-flux SU(4) Hubbard model on a square lattice. *Phys. Rev. B* **97**, 195122 (2018).

47. Larsen, C. B. et al. Exact diagonalization study of the hubbard-parametrized four-spin ring exchange model on a square lattice. *Phys. Rev. B* **99**, 054432 (2019).

48. Matsuno, J. et al. Engineering a spin-orbital magnetic insulator by tailoring superlattices. *Phys. Rev. Lett.* **114**, 247209 (2015).

49. Hao, L. et al. Novel spin-orbit coupling driven emergent states in iridate-based heterostructures. *J. Phys. Chem. Solids* **128**, 39–53 (2019).

50. Liu, X. et al. Interfacial charge-transfer mott state in iridate-nickelate superlattices. *Proc. Natl Acad. Sci.* **116**, 19863–19868 (2019).

51. Nelson, J. N. et al. Interfacial charge transfer and persistent metallicity of ultrathin $SrIrO_3/SrRuO_3$ heterostructures. *Sci. Adv.* **8**, eabj0481 (2022).

52. Gruenewald, J. H. et al. Engineering 1D quantum stripes from superlattices of 2D layered materials. *Adv. Mater.* **29**, 1603798 (2017).

53. Kim, J. et al. Single crystal growth of iridates without platinum impurities. *Phys. Rev. Mater.* **6**, 103401 (2022).

54. Kim, J.-K. et al. Resonant Inelastic X-ray scattering endstation at the 1C beamline of pohang light source II. *J. Synchrotron Radiat.* **30**, 643–649 (2023).

Acknowledgements

Author contributions

Competing interests

Additional information